Monthly Notices of the ROYAL ASTRONOMICAL SOCIETY

MNRAS **495,** 3538–3550 (2020) doi:10.1093/mnras/staa1356

# Reobserving the NLS1 galaxy RE J1034+396 – I. The long-term, recurrent X-ray QPO with a high significance

Chichuan Jin [1,2★] Chris Done[3] and Martin Ward[3]

[1]*National Astronomical Observatories, Chinese Academy of Sciences, 20A Datun Road, Beijing 100101, China*
[2]*School of Astronomy and Space Sciences, University of Chinese Academy of Sciences, 19A Yuquan Road, Beijing 100049, China*
[3]*Centre for Extragalactic Astronomy, Department of Physics, University of Durham, South Road, Durham DH1 3LE, UK*

Accepted 2020 May 11. Received 2020 April 12; in original form 2020 January 6

## ABSTRACT

RE J1034+396 is a narrow-line Seyfert 1 galaxy (NLS1) in which the first significant X-ray quasi-periodic oscillation (QPO) in an active galactic nucleus (AGN) was observed in 2007. We report the detection of this QPO in a recent *XMM–Newton* observation in 2018 with an even higher significance. The quality factor of this QPO is 20, and its period is 3550 ± 80 s, which is 250 ± 100 s shorter than in 2007. While the QPO's period has no significant energy dependence, its fractional root mean square variability increases from 4 per cent in 0.3–1 keV to 12 per cent in 1–4 keV bands. An interesting phenomenon is that the QPO in 0.3–1 keV *leads* that in the 1–4 keV bands by 430 ± 50 s with a high coherence, opposite to the soft X-ray *lag* reported for the observation in 2007. We speculate that the QPO has an intrinsic hard lag, while the previous reported soft lag is caused by the interference of stochastic variability. This soft X-ray lead in the new data supports the idea that the QPO of RE J1034+396 is a possible AGN counterpart of the 67 Hz high-frequency QPO seen in the black hole binary GRS 1915+105. We also search for QPO harmonics, but do not find any significant signals. Our new data reinforce previous results that the QPO is seen in a specific spectral state, as the only two observations showing no significant QPO signal exhibit an even stronger soft X-ray excess than the other six observations that display the QPO. Therefore, our results imply that the QPO in RE J1034+396 is physically linked to a soft X-ray component.

**Key words:** accretion, accretion discs – galaxies: active – galaxies: nuclei – galaxies: Seyfert.

## 1 INTRODUCTION

### 1.1 X-ray QPO in AGN

Both stellar mass black hole binaries (BHBs) and active galactic nuclei (AGNs) are powered by gas accreting on to a central black hole, and their observational properties are determined primarily by the black hole mass, mass accretion rate and spin. This relative simplicity should allow us to scale their observed X-ray properties such as variability and spectra between these two very different black hole mass systems. However, while the broad-band power spectral densities (PSD) do show some similarities (McHardy et al. 2006, 2007), the BHB show strong quasi-periodic oscillations (QPOs) at both low frequencies (0.1–10 Hz: potentially from Lense–Thirring precession: Stella & Vietri 1998; Ingram, Done & Fragile 2009; Veledina, Poutanen & Ingram 2013) and high frequencies (hundreds of Hz: potentially related to the Keplerian period of the innermost disc: Remillard & McClintock 2006), which are generally absent in AGNs.

The lack of QPO detections in AGNs is probably mainly due to the much longer time-scale of AGN QPO predicted by scaling there from BHB. Even the lowest mass AGN of $\sim 10^6$ $M_\odot$ would have predicted mass-scaled low-frequency QPOs at 0.1–10 d time-scales, which makes them difficult to study with the restricted duration of continuous X-ray exposures (Vaughan & Uttley 2005, 2006). More typical local AGNs with masses of $\sim 10^{7-8}$ $M_\odot$ would imply much worse data windowing problems. Instead, high-frequency QPOs provide a better potential match to observational constraints for the lowest mass AGN. These are observed locally as narrow-line Seyfert 1 galaxies (NLS1s), which are accreting at high Eddington ratios (e.g. Done & Jin 2016; Jin, Done & Ward 2016, 2017a,b). Indeed, the first AGN X-ray QPO was discovered in the NLS1 RE J1034+396 with a period of 3730 ± 60 s (Gierliński et al. 2008). Since then a few X-ray QPOs with lower significances have been reported in NLS1s, such as 1H 0707−495 (Pan et al. 2016; Zhang et al. 2018), MS 2254.9−3712 (Alston et al. 2015), Mrk 766 (Zhang et al. 2017), MCG-06-30-15 (Gupta et al. 2018). A couple of Seyfert 2s were also reported to exhibit a QPO, including 2XMM J123103.2+110648 (Lin et al. 2013) and XMMU J134736+173403 (Carpano & Jin 2018). X-ray QPOs were reported in tidal disruption events around supermassive black holes, such

★ E-mail: ccjin@bao.ac.cn

as Swift J164449.3+573451 (Reis et al. 2012) and ASASSN-14li (Pasham et al. 2019). Recently, a new type of X-ray periodic signal given the term quasi-periodic eruption (QPE) has been reported in the Seyfert 2 galaxy GSN 069, whose black hole mass is estimated to be $\sim 4 \times 10^5$ $M_\odot$ (Shu et al. 2018; Miniutti et al. 2019), although the properties of X-ray QPE are very different from QPO.

### 1.2 RE J1034+396

RE J1034+396 is a well-studied AGN located at $z = 0.042$. It has an extraordinary steep soft X-ray spectrum compared to other AGNs (Puchnarewicz et al. 1995; Wang & Netzer 2003; Casebeer et al. 2006; Crummy et al. 2006) though much of this is probably due to the disc itself (Done et al. 2012; Jin et al. 2012a,b,c). The hydrogen Balmer emission lines of RE J1034+396 have a full width at half-maximum (FWHM) of $\lesssim$1500 km s$^{-1}$, defining the source as an NLS1 galaxy (Puchnarewicz et al. 1995; Mason, Puchnarewicz & Jones 1996; Gonçalves, Véron & Véron-Cetty 1999; Bian & Huang 2010). Its black hole mass is estimated to be $10^6$–$10^7$ $M_\odot$ (see Czerny et al. 2016 for a summary of several different mass estimates), with the most probable mass range being (1–4) $\times$ $10^6$ $M_\odot$ (Gierliński et al. 2008; Middleton et al. 2009; Bian & Huang 2010; Jin et al. 2012a; Chaudhury et al. 2018). The mass accretion rate of RE J1034+396 is close to or slightly above the Eddington limit (Jin et al. 2012a; Czerny et al. 2016).

The most notable phenomenon of RE J1034+396 is the QPO signal detected in its X-ray emission, which is the first significant detection of an X-ray QPO in AGN (Gierliński et al. 2008). Since then many studies have been conducted in order to understand the physical origin of this QPO, as well as its potential trigger. The QPO varies significantly in its root mean square (rms) amplitude between different observations, but not in its frequency. The QPO signal was most significant in the first detection during the *XMM–Newton* observation in 2007 (Gierliński et al. 2008; Middleton et al. 2009). Then it was detected in only four of the six subsequent *XMM–Newton* observations made before 2011 (Alston et al. 2014). The high coherence of this QPO signal ($Q \gtrsim 10$) is comparable to the high-frequency QPO at 67 Hz seen in the high-mass accretion rate state of the BHB GRS 1915+105 ($M = 12.4^{+2.0}_{-1.8}$ $M_\odot$, Reid et al. 2014). This is also consistent with the mass scaling if the mass of RE J1034+396 is (1–4) $\times$ $10^6$ $M_\odot$ (Middleton, Uttley & Done 2011; Czerny et al. 2016; Chaudhury et al. 2018).

The rms of the QPO is energy dependent, showing that the QPO spectrum is subtly different to the time-averaged spectrum, and the hard X-ray QPO leads the soft X-ray by 300–400 s (Gierliński et al. 2008; Middleton, Done & Uttley 2011). This corresponds to a light travel distance of $\sim$30 $R_g$ in the disc reprocessing scenario, which however places no constraints on the black hole spin. This soft X-ray lag was also reported by Zoghbi & Fabian (2011) who performed spectral-timing analysis in the frequency domain using the same data set.

### 1.3 This work

Despite all previous studies, the long-term behaviour (over a time-scale of 10 yr) of the QPO in RE J1034+396 remains unknown. This is because of the visibility issue of this source with *XMM–Newton* since 2011. In this paper, we present results from our new *XMM–Newton* observation of RE J1034+396 obtained in 2018. These new data allow us to explore the latest properties of this QPO signal, and help us to understand the mechanism of AGN QPO in general.

This paper is organized as follows. In Section 2, we list all the *XMM–Newton* observations of RE J1034+396 and describe the data reduction procedures. In Section 3, we present the light curve and QPO signal in the new data, which is followed by a detailed analysis and modelling of the PSD and QPO in Section 4. The study of the QPO's long-term variation is presented in Section 5. Detailed discussions of the QPO mechanism are presented in Section 6, and the final section summarizes our main results and conclusions. Unless otherwise specified, all the error bars presented in this work refer to the 1$\sigma$ uncertainty.

## 2 OBSERVATIONS AND DATA REDUCTION

RE J1034+396 was previously observed by *XMM–Newton* (Jansen et al. 2001) for eight times between 2002 and 2011, after which it was no longer observed by *XMM–Newton* due to restricted visibility, and so the QPO signal could not be monitored. Since 2018 the visibility has improved to $\gtrsim$70 ks per *XMM–Newton* orbit, and so we observed it again with *XMM–Newton* in 2018 for 72 ks in order to re-examine its X-ray QPO. This new observation is already 7 yr from the previous observation in 2011, and 11 yr from the initial discovery of QPO in 2007. All of the observations are listed in Table 1.

We downloaded all the data from *XMM–Newton* Science Archive (XSA). In this study, we mainly focused on the X-ray variability and QPO, so only the data from the European Photon Imaging Cameras (EPIC; Strüder et al. 2001) were used. The *XMM–Newton* Science Analysis System (SAS v18.0.0) was used to reduce the data. First, the EPPROC and EMPROC tasks were used to reprocess the data with the latest calibration files. Then we defined a circular region with a radius of 80 arcsec centred on the position of RE J1034+396 as the source extraction region. In the first two observations the EPIC cameras were in the full-window mode, so the background extraction region was chosen to be the same size in a nearby region without any sources. Later observations were all taken in the small-window mode, so for the two metal oxide semiconductor (MOS) cameras we extracted the background from a nearby charge-coupled device (CCD) chip, while for the pn camera the background was extracted close to the edge of the small window to minimize contamination of the primary source. We adopted good events (FLAG = 0) with PATTERN $\leq$ 4 for pn and PATTERN $\leq$ 12 for MOS1 and MOS2.

The EVSELECT task was used to extract the source and background light curves, where the background flares were identified. By running the EPATPLOT task, we found that the first two observations in the full-window model suffered from significant photon pile-up in the central $\sim$10 arcsec region of the point spread function (PSF), while the following observations were not affected by this effect due to the small-window mode used. The EPICLCCORR task was used to perform the background subtraction, and apply various corrections to produce the intrinsic source light curve. The source and background spectra were also extracted using the EVSELECT task. Then the ARFGEN, RMFGEN, and GRPPHA tasks were run to produce the auxiliary and response files and rebin the spectra. The XSPEC software (v12.10.1, Arnaud 1996) was used to perform all the spectral analysis. All the timing results presented in this paper were based on the EPIC-pn data with the highest signal to noise (S/N) among the three EPIC cameras. The MOS data were reduced in a similar way and used for the consistency check.

**Table 1.** List of *XMM–Newton* observations on RE J1034+396. GTI is the integrated good exposure time in EPIC-pn after removing intervals containing background flares. Obs-1 and Obs-2 are in the full-frame mode, while the other observations are all in the small-window mode. $N_{\rm H,host}$ is the best-fitting host galaxy absorption (see Section 5.3), and the Galactic absorption is fixed at $1.36 \times 10^{20}$ cm$^{-2}$. $F_{0.3-2\rm keV}$ is the absorbed 0.3–2 keV flux. Errors indicate the 90 per cent confidence range. $f_{\rm QPO}$ and $Q_{\rm QPO}$ are the QPO frequency and quality factor in the 1–4 keV band as reported by Alston et al. (2014) for the first eight observations. The data of Obs-1 are not good enough for the QPO analysis due to severe background contamination. Obs-3 and Obs-6 are the two observations when the QPO is not detected. Obs-9 is our new observation.

| Obs No. | ObsID | Obs date | On-time (ks) | GTI (ks) | $N_{\rm H,host}$ ($10^{20}$ cm$^{-2}$) | $F_{0.3-2\rm keV}$ ($10^{-12}$ erg cm$^{-2}$ s$^{-1}$) | $F_{2-10\rm keV}$ | $\Gamma_{0.3-2\rm keV}$ | $\Gamma_{2-10\rm keV}$ | $f_{\rm QPO}$ ($10^{-4}$ Hz) | $Q_{\rm QPO}$ |
|---|---|---|---|---|---|---|---|---|---|---|---|
| Obs-1 | 0109070101 | 2002-05-01 | 12.8 | 1.8 | $0.00^{+0.58}_{l}$ | $8.72^{+0.29}_{-0.29}$ | $0.95^{+0.39}_{-0.39}$ | $3.86^{+0.05}_{-0.05}$ | $1.91^{+0.37}_{-0.27}$ | – | – |
| Obs-2 | 0506440101 | 2007-05-31 | 91.1 | 79.5 | $1.00^{+0.16}_{-0.16}$ | $8.52^{+0.04}_{-0.04}$ | $1.16^{+0.04}_{-0.04}$ | $3.81^{+0.01}_{-0.01}$ | $2.06^{+0.06}_{-0.06}$ | 2.7 | 24 |
| Obs-3 | 0561580201 | 2009-05-31 | 60.8 | 43.4 | $1.08^{+0.11}_{-0.11}$ | $11.27^{+0.04}_{-0.04}$ | $0.82^{+0.03}_{-0.03}$ | $4.20^{+0.01}_{-0.01}$ | $2.09^{+0.05}_{-0.05}$ | × | × |
| Obs-4 | 0655310101 | 2010-05-09 | 44.3 | 19.3 | $0.00^{+0.17}_{l}$ | $7.97^{+0.05}_{-0.05}$ | $1.07^{+0.05}_{-0.05}$ | $3.73^{+0.01}_{-0.01}$ | $2.03^{+0.06}_{-0.06}$ | 2.7 | 11 |
| Obs-5 | 0655310201 | 2010-05-11 | 53.0 | 31.2 | $0.00^{+0.18}_{l}$ | $7.92^{+0.04}_{-0.04}$ | $1.13^{+0.04}_{-0.04}$ | $3.71^{+0.01}_{-0.01}$ | $1.97^{+0.05}_{-0.05}$ | 2.5 | 13 |
| Obs-6 | 0675440301 | 2011-05-07 | 32.2 | 18.2 | $2.29^{+0.16}_{-0.16}$ | $13.56^{+0.07}_{-0.07}$ | $1.02^{+0.05}_{-0.05}$ | $4.40^{+0.01}_{-0.01}$ | $1.96^{+0.06}_{-0.06}$ | × | × |
| Obs-7 | 0675440101 | 2011-05-27 | 36.0 | 14.7 | $0.01^{+0.26}_{-0.01}$ | $8.91^{+0.07}_{-0.07}$ | $1.20^{+0.07}_{-0.07}$ | $3.86^{+0.01}_{-0.01}$ | $1.97^{+0.07}_{-0.07}$ | 2.6 | 9 |
| Obs-8 | 0675440201 | 2011-05-31 | 29.4 | 12.6 | $0.04^{+0.27}_{-0.04}$ | $8.12^{+0.07}_{-0.07}$ | $1.24^{+0.07}_{-0.07}$ | $3.73^{+0.01}_{-0.01}$ | $1.87^{+0.07}_{-0.07}$ | 2.6 | 7 |
| Obs-9 | 0824030101 | 2018-10-30 | 71.6 | 64.7 | $0.00^{+0.02}_{l}$ | $7.99^{+0.03}_{-0.03}$ | $1.09^{+0.03}_{-0.03}$ | $3.73^{+0.01}_{-0.01}$ | $2.01^{+0.05}_{-0.05}$ | 2.8 | 20 |

## 3 THE NEW *XMM–Newton* OBSERVATION IN 2018

We first explore the X-ray variability of RE J1034+396 during the latest *XMM–Newton* observation, and search for a QPO signal in the light curve.

### 3.1 X-ray light curves

RE J1034+396 exhibits significant X-ray variability in the latest *XMM–Newton* observation in 2018 (hereafter: Obs-9), as shown by the EPIC-pn light curves in Fig. 1. The shadowed regions in the figure indicate time intervals affected by background flares. For ∼90 per cent of the observing time the background was very low and stable, only the first ∼ 4 ks and a few short periods are affected by flares, so the overall data quality is excellent. After masking out all of the background flares, the mean source count rates are found to be 4.55, 0.52, and 0.14 counts per second (cps) in the three typical energy bands of 0.3–1, 1–4, and 2–10 keV, respectively. This immediately suggests that the X-ray spectrum of RE J1034+396 remained soft during the new observation. These energy bands are representative because the 0.3–1 keV band is dominated by the soft excess, and the 2–10 keV band is dominated by the hard X-ray corona emission (e.g. Middleton et al. 2009). The 1–4 keV band is chosen to facilitate comparison with previous studies, because the QPO signal was significantly detected in this band in five out of all eight *XMM–Newton* observations before 2011 (Alston et al. 2014). In Fig. 1, from the *y*-axis of fractional count rate relative to the mean value, it is also clear that the amplitude of the hard X-ray variability is much larger than that in the soft X-ray band, but the soft X-rays seem to have stronger variability over long time-scales (>1 ks) than short time-scales (<1 ks).

We apply the Ensemble Empirical Mode Decomposition (EEMD) method (Huang et al. 1998; Wu & Huang 2009; Hu et al. 2011) to these light curves in order to examine the variability in different time-scales. This method works in the time domain to resolve a noisy light curve into a complete set of independent components, namely the intrinsic mode functions (IMFs), which possess different variability patterns and are locally orthogonal to each other. This method has been previously applied to the light curve of RE J1034+396 for Obs-2, and the QPO variability is found to concentrate in one of the IMFs (Hu et al. 2014).

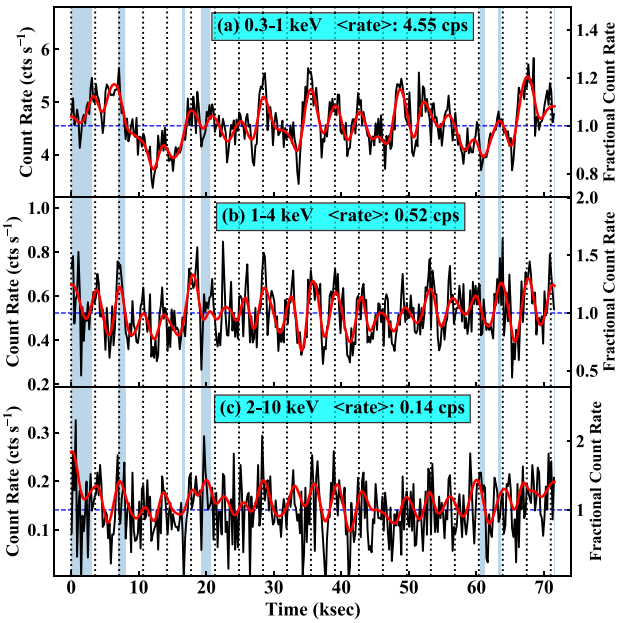


**Figure 1.** Light curves of RE J1034+396 in Obs-9 as observed by *XMM–Newton* EPIC-pn, binned with 200 s. In each panel, the shadowed regions indicate masked time intervals due to background flares. The red solid line is the summation of IMFs whose time-scales are equal or longer than the QPO period (see Section 3.1). The vertical dotted lines indicate every 3550 s time interval, which is the latest period of the 0.3–10 keV light curve.

The PYTHON PYEMD package was used to perform the EEMD analysis. We find that each light curve (50 s binned) can be decomposed into nine IMFs, with the time-scale increasing from the first component (C1) to the last (C9). We also find that the QPO signal is contained in C5, while C6 to C9 can be combined to show the variability over longer time-scales. The summation of IMFs whose time-scales are equal or longer than the QPO period is shown in Fig. 1 as the solid red line. The periodic positions separated by 3550 s (see Section 5.1) are marked by the vertical dotted lines. It is clearly seen that the instantaneous period of the QPO is varying within the observing time, confirming that it is indeed a quasi-periodic signal.

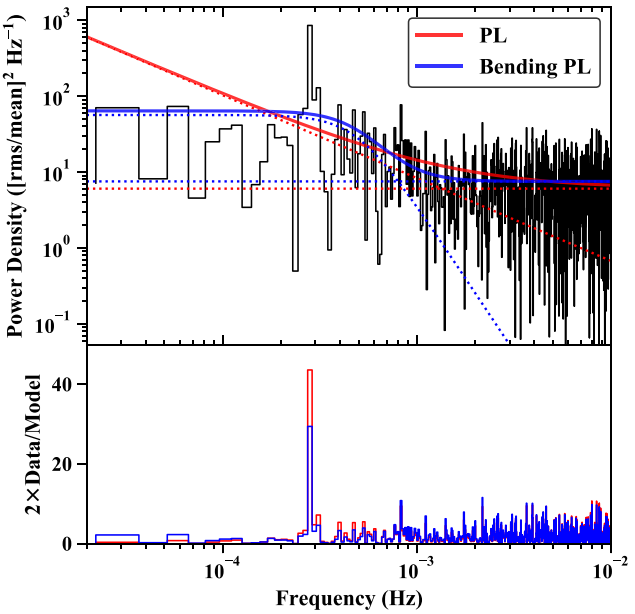


**Figure 2.** The 1–4 keV PSD of RE J1034+396 in Obs-9, fitted with a single power-law model (RL, red), or a bending power-law model (bending PL, blue). The high frequency range is dominated by the Poisson noise power, which is modelled as a free constant. The solid and dash lines indicate the total models and their separate components. The lower panel shows the data-to-model ratio (times by 2) versus frequency, where the QPO feature is clearly visible in both models.

### 3.2 X-ray PSD and the QPO signal

In order to quantitatively measure the QPO signal, we perform analysis in the frequency domain. We first produce the PSD[1] for the 1–4 keV light curve, where the QPO appears more significant than in other bands (Alston et al. 2014). The first 4 ks data are excluded because of the severe background contamination. The normalization of these PSD is chosen such that the integration of the PSD is the fractional rms variability (i.e. the Belloni–Hasinger normalization, Belloni & Hasinger 1990). Indeed, a strong peak feature can be identified in the PSD, as shown in Fig. 2. The frequency of this feature is similar to previously reported values (Alston et al. 2014), implying that it should be the same QPO signal as found in observations before 2011. The QPO feature is very narrow, although there appears to be a broader base which may be partly due to the fluctuation of the underlying red noise. For the width of the smallest frequency sampling interval, the quality factor of the QPO is 20 in the 1–4 keV band, suggesting that this QPO signal is highly coherent.

#### *3.2.1 Testing continuum-only hypothesis for the PSD*

We then perform some null hypothesis tests. First, we fit a single power-law model to the PSD using the maximum likelihood estimate (MLE) method (Vaughan 2010). Under the Belloni–Hasinger normalization, the theoretical Poisson power is a constant value, so we add a free constant to the power law and let the fitting determine the Poisson power. The red lines in the upper panel of Fig. 2 show the best-fitting PSD model and the separate components. The power-law slope is found to be $-1.09$. The Poisson noise power dominates above $10^{-3}$ Hz, while the red noise power dominates lower frequencies. A standard way to estimate the significance of the observed power, $I_j$, deviation from the model continuum, $S_j$, at any frequency $f_j$ is $R_j = 2I_j/S_j$. This can be used to make a test statistic $T_R = \max(R_j)$. This is shown in the lower panel of Fig. 2. The QPO is obvious, with the observed $T_R$ being 43.6.

However, this does not simply give a significance of the QPO via the $\chi^2$ distribution with two degrees of freedom (dof) of the observed power $I_j$, because there are also uncertainties in the model $S_j$ which should be taken into account. Instead, we follow the more robust Bayesian prescription of Vaughan (2010) which includes the uncertainty of estimating the intrinsic PSD parameters in the simulated *posterior* predictive periodograms.

We simulate the continuum model using the initial values of the MLE parameters, assuming a uniform prior probability density function (Vaughan 2010; Alston et al. 2014). The PYTHON EMCEE package is used to perform the Markov Chain Monte Carlo (MCMC) sampling in order to draw from the *posterior* of model parameters (Hogg, Bovy & Lang 2010). We generate $10^5$ *posterior* predictive periodograms, and fit each of them with the same model. Then the *posterior* predictive distributions (PPDs) are derived for $T_R$. These are shown in Fig. 3(a1). The *posterior* predictive $p$-value of $T_R$ is $< 10^{-5}$, i.e. none of the simulated periodograms can produce a larger $T_R$ than the observation.

These same simulations also allow us to assess the overall goodness of fit of the power-law continuum model to the data. The fit has overall $\chi^2 = 1053.5$, so this sum of squared standard errors can be used as a test statistic $T_{SSE} = \chi^2$. The PPDs of $T_{SSE}$ are shown in Fig. 3(a2). The *posterior* predictive $p$-value of $T_{SSE}$ is $< 10^{-5}$, i.e. none of the simulated periodograms can produce a larger $T_{SSE}$. These results clearly rule out the power-law continuum-only null hypothesis.

The X-ray PSD of AGNs often shows a break at high frequencies (McHardy et al. 2006, 2007). Vaughan (2010) shows that a bending power law is a better fit than a power law for the PSD of RE J1034+396, when the QPO feature is not modelled separately. Thus we replace the power-law model with a bending power law[2], and repeat all the above analysis. The MLE bend frequency is $4.9 \times 10^{-4}$ Hz. This slightly reduces $T_R$ to 29.4 i.e. the QPO significance is still high, but has more impact on the overall fit quality, with the $T_{SSE}$ being 812.4. The PPDs of $T_R$ and $T_{SSE}$ are shown in Figs 3(b1) and (b2). The *posterior* predictive $p$-values for the two statistics are 0.00018 and 0.054. The bending power-law model does give a better overall fit to the PSD which is within the 95 per cent confidence limit, but the deviation at the QPO frequency is still significant at the 0.00018 level.

Therefore, we can conclude that neither a power-law nor a bending power-law model can fully describe the PSD of RE J1034+396. The peak feature in $(2.5-3.5) \times 10^{-4}$ Hz is clearly an intrinsic signal in the PSD. Therefore, it would not be appropriate to include this feature in the PSD's continuum fitting, and the previous suggestion regarding the bending power law being preferred over a power law is no longer valid. Indeed, if we mask out this band from the fitting, we find that there is no statistical difference between a power law and a bending power law. Below we show the results when this QPO-like feature is modelled independently.

[1]This is actually a periodogram, which is a single realization of the intrinsic PSD. In this work we simply call it a PSD.

[2]A lower limit of 0 is put to the low-frequency slope of the bending power-law model in order to maintain a realistic PSD shape of AGN.

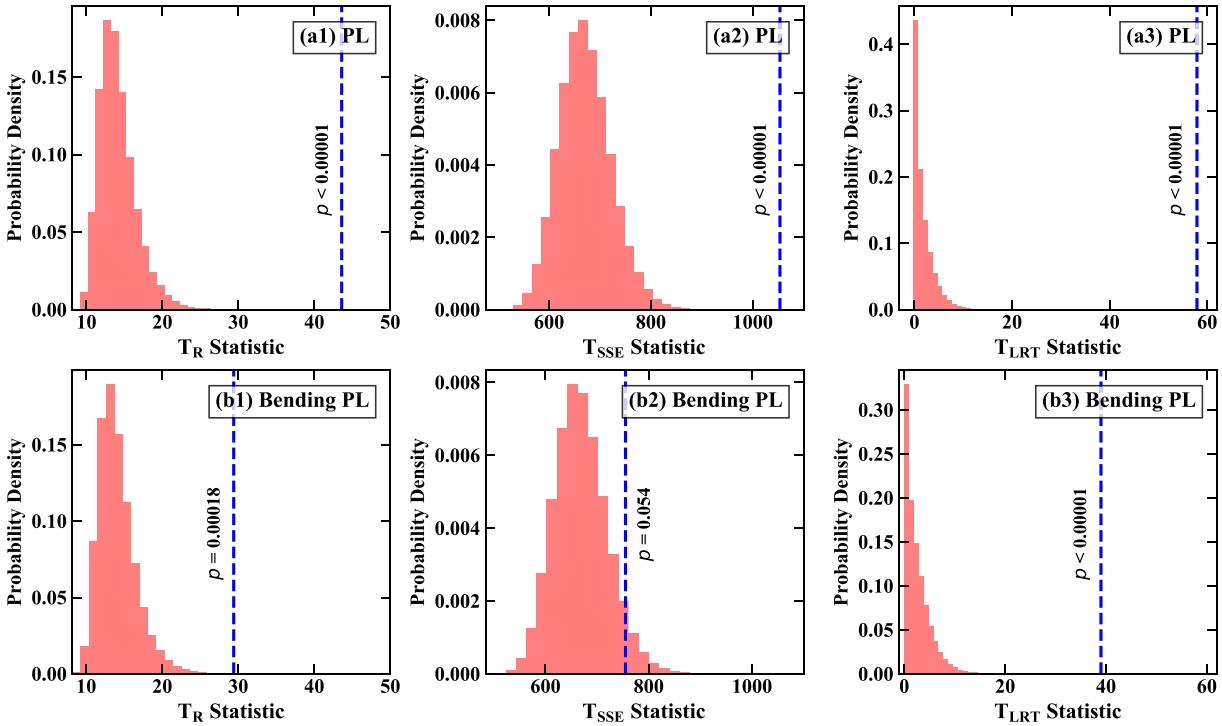


**Figure 3.** PPDs of the $T_R$ and $T_{SSE}$ statistics for the power-law model (PL) and the bending power-law model (bending PL) for the 1–4 keV PSD of RE J1034+396 in Obs-9. The $T_{LRT}$ statistic is for checking the decrease of deviance after adding a Lorentzian component to the continuum model to fit the QPO feature. The observed value is shown by the vertical blue dash line, together with the corresponding *posterior* predictive *p*-value. These results suggest that the QPO feature seen in Fig. 2 should be an intrinsic component of the PSD.

### 3.2.2 *More complete PSD models*

We now add a Lorentzian component to the model to describe the QPO-like feature, and test for the significance of this additional component using a likelihood ratio test statistic, $T_{LRT}$, which is derived from the difference in $\chi^2$ between the model with and without the Lorentzian. We emphasize that our application of $T_{LRT}$ does not require the two models to be nested (Vaughan 2010). $T_{LRT}$ is found to be very large for the power-law continuum, with a value of 57.9. The previous MCMC simulations of models for the continuum were fit with both a continuum and a continuum plus Lorentzian component, and the PPD for the change in $\chi^2$ for a model including a Lorentzian is shown in Fig. 3(a3) for the power law and (b3) for the bending power law. Both have *posterior* predictive *p*-values of $T_{LRT} < 10^{-5}$, This shows that a PSD model with a separate QPO component is significantly better than a continuum-only model at the level of $< 10^{-5}$.

As a further test, we also compare the goodness of fit between the power law plus Lorentzian and the previous bending power-law-only model. The observed $T_{LRT}$ between these two models is 23.1, with the bending power-law-only model being the less preferred model. Then we perform $10^5$ simulations of the *posterior* predictive periodograms using the bending power-law-only model. For all the simulated periodograms, the bending power-law-only model is always better than the power law plus Lorentzian model. Hence this is further evidence that the observed PSD must be very different from a single bending power law.

In addition to the above statistical tests, it is also important to emphasize that so far this QPO has been repeatedly detected at similar frequencies in six out of nine independent *XMM–Newton* observations (see Table 1), hence it must surely be a real signal intrinsic to the source, rather than a temporary feature due to the fluctuation of the underlying red noise.

In order to model these PSDs, we first need to decide which PSD continuum model to use. Previous works reported that for RE J1034+396 a bending power-law model fits the PSD better than a single power-law model (Vaughan 2010; Alston et al. 2014). However, it is important to realize that the bending of the power law was mainly driven by the QPO feature which was never modelled as a separate component. But now the QPO is confirmed to be an intrinsic PSD component, we should include it in the model and test the continuum PSD model again.

We compare the power-law model with a bending power law under the condition that the QPO is additionally modelled by a separate Lorentzian. In this case, the $T_{LRT}$ statistic between the two models is only 11.5, which corresponds to a *posterior* predictive *p*-value of 0.07. This indicates that the difference between the two model fits is not very significant. Also, the best-fitting bend frequency is found to be $9.7 \times 10^{-4}$ Hz. This frequency is two orders of magnitude higher than $1.7 \times 10^{-5}$ Hz, which is estimated from the correlation between the break frequency, black hole mass, and optical luminosity of AGNs (McHardy et al. 2006), for a black hole mass of $2 \times 10^6$ $M_\odot$ and optical luminosity of $2 \times 10^{43}$ erg $s^{-1}$ (Jin et al. 2012a). A similar low break frequency at $\sim 10^{-5}$ Hz is also seen in Chaudhury et al. (2018) in their longer time-scale broad-band PSD of RE J1034+396. Thus it is unlikely that this best-fitting bend is an intrinsic feature of the PSD, especially as it is not present in any of the other energy bands (see Figs 4a and c) or previous observations (Alston et al. 2014). Hence, we adopt a PSD model of POWERLAW + LORENZIAN + CONSTANT for all the subsequent fits.

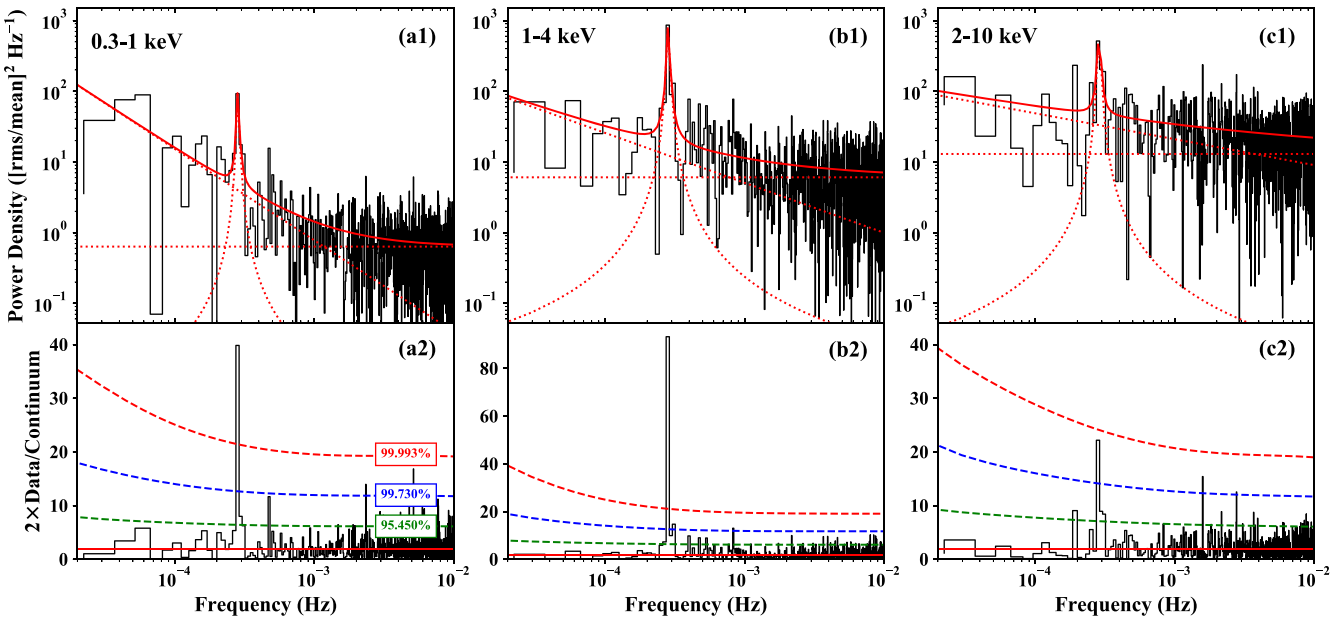


**Figure 4.** PSDs of RE J1034+396 in the 0.3–1, 1–4, and 2–10 keV bands, respectively. In (a1), the red solid line indicates the best-fitting model that is decomposed into three red dotted lines, including a power law to fit the intrinsic underlying noise, a free constant to fit the Poisson noise, and a Lorentzian profile to fit the QPO signal. In (a2), the ratio of the PSD data to the best-fitting PSD continuum is shown. A strong and coherent QPO peak can be seen at $\sim 2.8 \times 10^{-4}$ Hz (see Table 3 for more accurate values). The green, blue, and red dashed lines indicate the $2\sigma$, $3\sigma$, and $4\sigma$ confidence limits of the fluctuation in the red noise, respectively, with the model assuming that the QPO is a real PSD component superposed on the red noise continuum (see Section 4.1).

## 4 DETAILED PSD AND QPO ANALYSES

### 4.1 Energy dependence of the PSD and QPO

In order to further explore the PSD and QPO, we examine their behaviours in different energy bands. First, we produce PSDs for the light curves in 0.3–1, 1–4, and 2–10 keV bands. The upper panels of Fig. 4 show that a QPO feature exists in the PSDs of all three energy bands at similar frequencies, and all of them appear very narrow. Then we fit these PSDs with the PSD model mentioned above. The MLE model fits are shown as the red lines in the upper panels of Fig. 4. The best-fitting parameters are determined by the MLE method and are listed in Table 3. The Poisson noise power is higher in harder X-rays because of the decreasing count rate.

The lower panels of Fig. 4 show the ratio $R_j = 2 \times I_j/S_j$, where $S_j$ is the continuum model only, i.e. the same power law plus Poisson constant but *without* including the Lorentzian. The $R_j$ value at the QPO frequency in the 1–4 keV band now increases to 93.3, higher than the value of 43.6 in the previous section due to the power-law continuum level being lower when the Lorentzian is separately modelled.

We perform Bayesian analysis on the continuum power law (plus noise) with MCMC sampling as in Section 3 to produce $10^5$ *posterior* predictive periodograms, and use these to put the $2\sigma$, $3\sigma$, and $4\sigma$ significance levels (dashed lines) on the lower panels of Fig. 4. Since we only have $10^5$ simulations, we cannot go beyond a probability of $10^{-5}$ i.e. $4.6\sigma$. However, we can assess the peak significance by scaling the PPD results e.g. for the 1–4 keV energy band, the $R$ values for $2\sigma$, $3\sigma$, and $4\sigma$ are 6.4, 12.6, and 21.1, respectively. By comparison, a standard $\chi^2$ distribution with 2 dof has $R$ values corresponding to these $\sigma$ levels of 6.2, 11.8, and 19.3, which are only slightly smaller than for the full simulations. The peak $R$ is 93.3 in this band, which is 4.4× larger than the $R$ value at $4\sigma$. For a standard $\chi^2$ distribution with 2 dof, a $R$ value which is 4.4× higher than that for $4\sigma$ would be a $9\sigma$ significance. We similarly assess the significance level of the QPO in the 0.3–1 keV band to be $5.7\sigma$, but for the 2–10 keV band the PPD directly give the significance as $3.8\sigma$. The $R$ values and significances for each energy band are listed in Table 2. We emphasize that the confidence limits for the $R$ value in Fig. 4 are used to assess the significance of the QPO at any particular frequency. Thus it is different from the $T_R$ test presented in the previous section, which is used to assess the significance of a QPO signal over the entire frequency band.

Note that before this study, the highest $R_{QPO}$ for RE J1034+396 was reported to be ∼60 for the 0.3–10 keV band in Obs-2 (Gierliński et al. 2008, using the same model of a power-law continuum plus Lorentzian and Poisson noise). Therefore, not only does our new observation demonstrate the long-term nature of the QPO, but it also finds the so-far highest level of significance for an X-ray QPO signal in all AGNs.

**Table 2.** The first row shows the $R_{QPO}$ value (i.e. 2 × data/continuum at the QPO frequency) measured in the PSD of RE J1034+396 in Obs-9. As shown in Fig. 4, we use a power law plus a Poisson noise constant and a Lorentzian profile to model the entire PSD. The critical $R_{QPO}$ values for different confidence limits are derived from our Bayesian PSD simulations. The final row shows the significance of the observed QPO.

| | 0.3–1 keV | 1–4 keV | 2–10 keV |
|---|---|---|---|
| $R_{QPO,obs}$ | 39.8 | 93.3 | 22.2 |
| $R_{QPO,2\sigma}$ | 6.4 | 6.4 | 7.1 |
| $R_{QPO,3\sigma}$ | 12.6 | 12.6 | 14.1 |
| $R_{QPO,4\sigma}$ | 21.4 | 21.1 | 24.1 |
| Sig. of $R_{QPO,obs}$ | $5.7\sigma$ | $9.0\sigma$ | $3.8\sigma$ |

**Table 3.** Results of the MLE fit and Bayesian analysis of the PSDs of RE J1034+396 in different energy bands. $f_{QPO}$ is the peak frequency of the best-fitting Lorentzian profile to the QPO. $W_{QPO}$ is the FWHM of the best-fitting QPO Lorentzian profile in the log–log space. $rms_{QPO}$ is the rms of the QPO by integrating the best-fitting Lorentzian profile. $\alpha_{pl}$ is the slope of the continuum noise fitted by a power law. Pos is the Poisson noise power. We also list values corresponding to the Bayesian mean, 5 per cent, and 95 per cent percentiles.

| Parameter | Method | 0.3–1 keV | 1–4 keV | 2–10 keV |
|---|---|---|---|---|
| $f_{QPO}$ | MLE | 2.83 | 2.83 | 2.87 |
| ($\times 10^{-4}$ Hz) | $1\sigma$ | 0.06 | 0.07 | 0.08 |
| | Mean | 2.80 | 2.82 | 2.91 |
| | 5 per cent | 2.63 | 2.67 | 1.26 |
| | 95 per cent | 2.96 | 2.97 | 7.40 |
| $W_{QPO}$ | MLE | 0.014 | 0.018 | 0.017 |
| Log (Hz) | Mean | 0.008 | 0.012 | 0.013 |
| | 5 per cent | 2.1E-7 | 2.0E-6 | 3.4E-9 |
| | 95 per cent | 0.044 | 0.057 | 0.074 |
| $rms_{QPO}$ | MLE | 4.0 | 12.4 | 10.8 |
| (per cent) | Mean | 4.1 | 12.3 | 11.0 |
| | 5 per cent | 1.5 | 6.7 | 4.7 |
| | 95 per cent | 6.8 | 19.1 | 17.4 |
| $\alpha_{pl}$ | MLE | − 1.29 | − 0.71 | − 0.37 |
| | Mean | − 1.39 | − 0.99 | − 0.52 |
| | 5 per cent | − 1.06 | − 0.37 | − 0.18 |
| | 95 per cent | − 1.71 | − 1.72 | − 0.96 |
| Pos | MLE | 0.63 | 6.05 | 12.95 |
| | Mean | 0.67 | 3.93 | 3.74 |
| | 5 per cent | 0.55 | 2.90 | 2.7E-3 |
| | 95 per cent | 1.37 | 17.9 | 24.8 |

We repeat the Bayesian analysis with MCMC sampling on the full PSD model (including the Lorentzian). We use these PPD to set the 5 per cent and 95 per cent uncertainty ranges on the MLE parameter values for the power spectral components, as detailed in Table 3. We show the full PPD for the QPO frequency in each energy band in Fig. 5(a). Clearly this is consistent across all energies, which is also confirmed by the overlap of the QPO frequency uncertainty ranges in Table 3.

Table 3 shows that the width of the QPO is very small ($\Delta \log f = 0.014$ in 0.3–1 keV), and is consistent with being the same across all energy bands. The table also shows that the fractional rms amplitude of the QPO increases significantly with energy, showing that a larger fraction of hard X-rays are varying at the QPO frequency than the soft X-rays. However, since the flux ratio between 0.3–1 and 1–4 keV is 7.5, the absolute rms amplitude of the QPO in 0.3–1 keV is actually larger than that in 1–4 keV by a factor of 2.4. The spectrum of the QPO will be examined in more detail in our next paper (Paper II).

Fig. 5(b) shows that the best-fitting power-law slopes systematically harden at higher energies, with $\alpha_{pl} = -1.29$ for 0.3–1 keV, −0.71 for 1–4 keV, and −0.37 for 2–10 keV. Only 0.3 per cent of the simulations in 0.3–1 keV have power spectra as hard as observed in 1–4 keV, and only 0.01 per cent simulations in 0.3–1 keV have power spectra as hard as those observed in 2–10 keV. These results confirm that the steepening of the PSD continual slope towards softer X-rays is an intrinsic property of RE J1034+396. However, the normalization of the power at low frequencies ($\sim 10^{-5}$ Hz) is ∼100 [rms per mean]$^2$ Hz$^{-1}$, similar at all energies (see Fig. 4), which suggests that the difference is in the amount of high frequency power.

Similar properties of the PSD continuum are also seen in other NLS1s (e.g. Jin et al. 2013; Jin, Done & Ward 2016, 2017a). This can be interpreted in a model where fluctuations propagate from the disc (which dominates at low energies) to the corona (which dominates at high energies), with additional fluctuations in the corona enhancing the high frequency power in the energy bands dominated by this component (e.g. Gardner & Done 2014).

### 4.2 Testing potential harmonics of the QPO signal

We also search for possible harmonics associated with this highly significant QPO. In BHBs, a high-frequency QPO may have harmonics at frequency ratios of 2:3, 3:5, and 2:5, and a low-frequency QPO may exhibit a harmonic frequency ratio of 1:2. Since it is not clear if the detected QPO in RE J1034+396 represents the fundamental or harmonic frequency, we check all possible harmonic frequencies for potential peak features. Based on the observed QPO frequency of $2.8 \times 10^{-4}$ Hz, the 2:3, 3:5, and 2:5 ratios predict potential peaks at $1.9 \times 10^{-4}$, $4.2 \times 10^{-4}$, $1.7 \times 10^{-4}$, $4.7 \times 10^{-4}$, $1.1 \times 10^{-4}$, and $7.0 \times 10^{-4}$ Hz. The 1:2 ratio predicts potential peaks at $1.4 \times 10^{-4}$ and $5.6 \times 10^{-4}$ Hz.

However, it is already clear from the lower panel of Fig. 4 that there are no features above $3\sigma$ significance at any other frequency in any of the energy bands. The strongest feature which is even close to any of the potential harmonics listed above is at $1.9 \times 10^{-4}$ Hz in the PSD of 2–10 keV band (see Fig. 4c), but this is only seen at $\sim 2.1\sigma$. No other energy bands show peaks with $> 2\sigma$ significance at any of the potential harmonic frequencies. The feature at $4.8 \times 10^{-4}$ Hz in the 0.3–1 keV band has $\sim 2.4\sigma$ significance, but this frequency is not harmonically related. No significant harmonics are seen in the Obs-2 data either (Gierliński et al. 2008; Vaughan 2010; Alston et al. 2014). Therefore, we conclude that there are no significant harmonics of the QPO signal in the current data of RE J1034+396.

The QPO of RE J1034+396 is often compared to the 67 Hz high-frequency QPO of the BHB GRS 1915+105, as it approximately scales with the mass difference between these two accreting black holes (Middleton et al 2009). The overall energy spectra of GRS 1915+105 in observations showing the 67 Hz are very similar to those of RE J1034+396 with a strong disc, a smaller warm Compton component, and an even smaller hot Compton tail (Middleton & Done 2010). GRS 1915+105 shows three harmonic peaks at 27 Hz (Belloni, Méndez & Sánchez-Fernández 2001), 34 Hz (Belloni & Altamirano 2013), and 40 Hz (Strohmayer 2001), but only the 34 and 41 Hz QPOs appear simultaneously with the 67 Hz QPO. The 34 Hz QPO has a fractional rms of 0.8 per cent and a quality factor of 13.1 in 2–15 keV. In comparison, the 67 Hz QPO has an rms of 2.0 per cent and a quality factor of 24.7 in the same energy band, and so the 34 Hz QPO is 60 per cent weaker than the 67 Hz QPO, but with a similar line width. The 41 Hz QPO has a fractional rms of 2.4 per cent and a quality factor of 7.7 in 13–27 keV, while in the same energy band the 67 Hz QPO has an rms of 1.9 per cent and a quality factor of 19.6, thus the 41 Hz QPO is 26 per cent more powerful than the 67 Hz QPO, but its profile is 56 per cent broader.

Assuming that the QPO of RE J1034+396 has similar harmonics as the 67 Hz QPO in GRS 1915+105, we can estimate that the intrinsic PSD of RE J1034+396 may have an extra peak at $1.4 \times 10^{-4}$ Hz with an rms of 5.0 per cent, or at $1.7 \times 10^{-4}$ Hz with an rms of 15.6 per cent. Such features are not observed in the PSDs of RE J1034+396 in Fig. 4. We test this explicitly using the 1–4 keV PSD. We add the expected harmonic at $1.4 \times 10^{-4}$ Hz to the best-fitting PDS model and simulate $10^5$ periodograms. Only a fraction 0.052 of the simulations with the harmonic have power

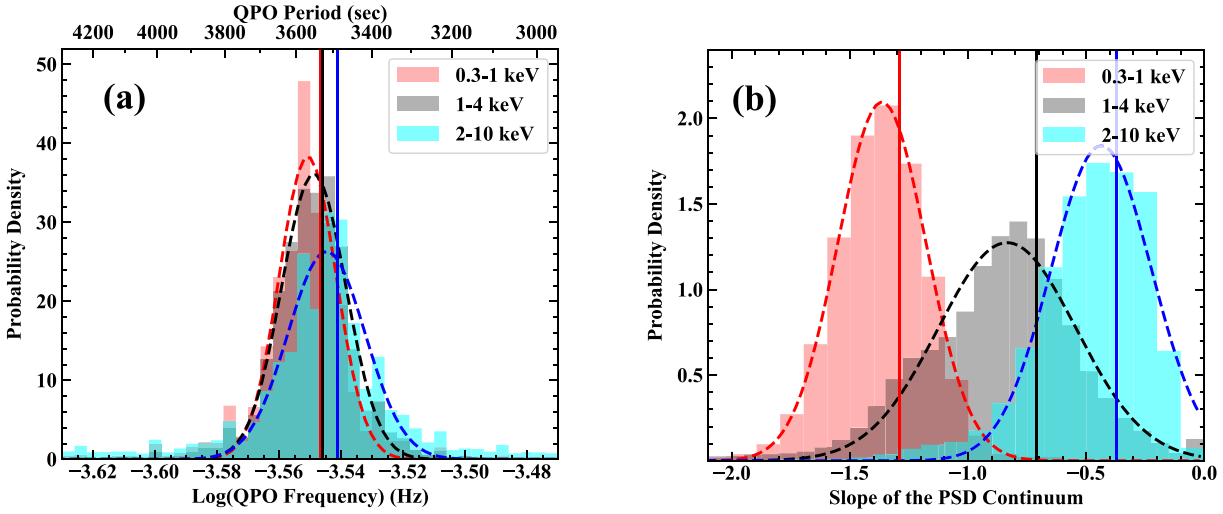


**Figure 5.** The PPDs of the QPO frequency (a) and the slope of the PSD continuum (b) in 0.3–1 (red histogram), 1–4 (black histogram), and 2–10 keV (cyan histogram). The best-fitting Gaussian profiles of these distributions are shown by the dash lines. The vertical solid lines mark the best-fitting MLE values (see Section 4.1 for detailed descriptions).

at that frequency as low as observed. We repeat the simulations for the potential harmonic at $1.7 \times 10^{-4}$ Hz, and find only a fraction 0.01 have power this small. Therefore, the non-detection of these two potential harmonics is probably not due to the random fluctuation of the PSD swamping the signal, but rather it is intrinsic to RE J1034+396. The above analysis rules out the presence of harmonics of similar relative strengths to those observed in GRS GRS 1915+105 in the current observation of RE J1034+396, but we cannot rule out the possibility that much weaker harmonics may exist, but are swamped by the PSD's fluctuation. Furthermore, GRS 1915+105 does not often exhibit the 67 Hz QPO and its harmonics simultaneously. Clearly we cannot exclude the possibility that future observations of RE J1034+396 may show these harmonics.

## 5 LONG-TERM VARIATION OF THE QPO

We compare some key properties of the QPO between Obs-9 and previous observations, especially Obs-2 where the background contamination is low and the QPO signal can be detected across the entire 0.3–10 keV band. Such a comparison allows us to verify the robustness of various QPO properties, as well as checking if there is any evidence for the long-term variation of the QPO.

### 5.1 Long-term variation of the QPO frequency

The QPO frequencies reported in previous observations are all in the range of $(2.5-2.7) \times 10^{-4}$ Hz (see Table 1), except for the new Obs-9, in which the frequency increases to $2.83 \times 10^{-4}$ Hz. Therefore, it is necessary to assess the significance of this difference. We only compare Obs-9 with Obs-2, because both of these two observations have low background, and the QPO signal is well determined. For Obs-2, Gierliński et al. (2008) reported that within the 23–83 ks data segment the QPO signal was more significant, thus we perform the comparison with the 0–83 and 23–83 ks data segments, separately. The data within 83–91 ks of Obs-2 are excluded because of the background contamination. Since the QPO frequency does not change significantly with the photon energy, we use the entire 0.3–10 keV data to achieve the best S/N in the light curve. The same Bayesian analysis is performed to derive the PPD of the QPO frequency.

Fig. 6 compares the QPO frequency between Obs-2 and Obs-9. In (a), we compare the data-to-model ratio around the QPO frequencies for the three data sets. In Obs-2, when the 0–83 ks data segment is used, two nearby QPO peaks can be detected. The stronger peak is at $2.63 \times 10^{-4}$ Hz, while the weaker one is at $2.42 \times 10^{-4}$ Hz. If the first 23 ks data are excluded, the lower frequency peak becomes much weaker. Hence, we think the low-frequency peak is mainly due to the instantaneous variation of the QPO period (Czerny et al. 2010; Hu et al. 2014). In comparison, the QPO in Obs-9 is clearly a single peak, and is shifted to a higher frequency. The histograms in (b) indicate the PPDs of the QPO frequency for the three data sets. The vertical solid lines indicate the best-fitting MLE values. For Obs-2 the best-fitting MLE period of QPO is $3920 \pm 150$ s in 0–83 ks, and $3800 \pm 70$ s in 23–83 ks, which are consistent with the results reported before (e.g. Gierliński et al. 2008; Alston et al. 2014; Hu et al. 2014). The QPO period in Obs-9 is, however, found to be $3550 \pm 80$ s, which is $250 \pm 100$ s (i.e. ∼7 per cent of the QPO period) smaller than in Obs-2. The difference between the PPDs of the two observations is also obvious. Compared to the PPD of the QPO frequency for the 0–83 ks segment of Obs-2, the QPO frequency in Obs-9 has a *posterior* predictive $p$-value of 0.019. For the 23–83 ks segment of Obs-2, the $p$-value is 0.028.

Based on these results, we report that the QPO frequency in Obs-9 is higher than that found in Obs-2. It is relevant to mention that the QPO also has a flickering nature within a single observation, and that the instantaneous period varies between 3000 and 4000 s (Hu et al. 2014). However, this does not mean that the observed long-term variation of the QPO frequency is simply due to the short-term variation. In fact, both Obs-2 and Obs-9 contain more than 20 QPO cycles, and so our comparison of the QPO frequency is statistically meaningful. However, it is not known if the increase of QPO frequency (e.g. the decrease of QPO period) within the last 11 yr is a monotonic trend or a fluctuation, because in the other observations the QPO signal was not well constrained due to poor data quality (Alston et al. 2014). Clearly, future *XMM–Newton* observations of RE J1034+396 can bring further evidence on the long-term variation of the QPO frequency, and hence help us to underlying physical mechanisms involved.

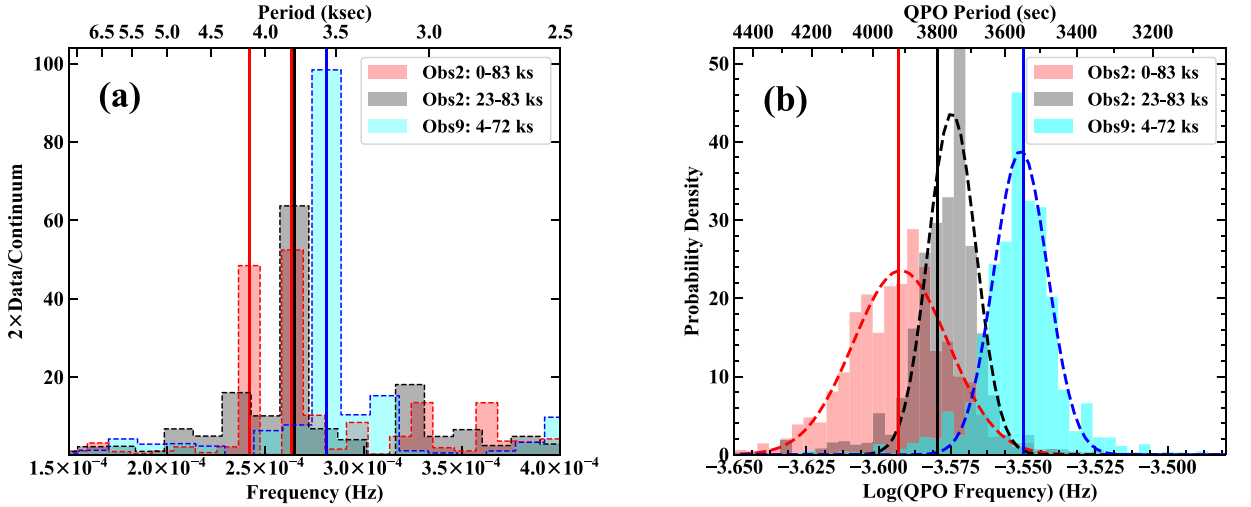


**Figure 6.** Comparison of the QPO frequency observed in Obs-2 and Obs-9 for the 0.3–10 keV band. (a): PSDs of different data segments relative to their best-fitting continuum model around the QPO frequency. Solid vertical lines indicate frequencies of different QPO peaks. Two nearby narrow QPO peaks are seen in the 0–83 ks data segment of Obs-2. (b): different histograms indicate the PPDs of the QPO frequency for different data segments. Dashed lines indicate the best-fitting Gaussian profiles. Vertical solid lines indicate the best-fitting MLE values.

### 5.2 Reversed QPO time lag between Obs-2 and Obs-9

Another important phenomenon related to the QPO is the phase lag (equation time lag in the time domain). Gierliński et al. (2008) applied the light-curve folding method and found ∼260 s lag between 0.3–0.4 and 2–10 keV (leading) in Obs-2. Middleton, Done & Uttley (2011) used the same data and method, and found ∼370 s lag between 0.2–0.3 and 1–10 keV (leading). However, we notice that this method is sensitive to the accuracy of the folding period. A more robust method is to perform the phase lag analysis in the Fourier domain (e.g. Uttley et al. 2014), because it differentiates the variability into different frequency bins. Zoghbi & Fabian (2011) applied this method to the Obs-2 data, and found a lag of ∼500 s between 0.4–0.6 and 1.5–2.0 keV (leading), with a coherence of ∼0.6 around the QPO frequency. They also showed that the lag spectrum does not change significantly with the inner radius of the annular source extraction region, thereby ruling out any significant influence from pile-up.

For consistency, we first reproduce the above results for Obs-2. Three inner radii ($r_s$) of the annular source extraction region are tested in order to check the effect of pile-up. The resultant lag versus frequency and coherence versus frequency plots are shown in Figs 7(a) and (c). The time lag and coherence values in the QPO frequency bin of $(2.5-3.5) \times 10^{-4}$ Hz are listed in Table 4. Our analysis confirm that in Obs-2 the QPO in 0.3–1 keV lags behind 1–4 keV by 200–300 s for all values of $r_s$ from 0 to 12.5 arcsec. As the S/N drops towards larger inner radii, the lag becomes less significant with larger errors and the coherence becomes smaller (see Table 4). However, even with $r_s = 0$ arcsec the lag is only detected at a significance of $2\sigma$.

We then investigate the time lag in Obs-9, but without trying different source extraction regions as these data are not affected by pile-up. The results for lag versus frequency and coherence versus frequency are shown in Figs 7(b) and (d). Surprisingly, we find that the lag in Obs-9 has an opposite direction from Obs-2, i.e. the QPO phase in the 1–4 keV band lags behind that in 0.3–1 keV band. The absolute lag value is 430 ± 50 s, which is much more significant than that found in Obs-2, and is also associated with a high coherence of 0.89 ± 0.06. Hence, the soft X-ray lead in Obs-9 is clearly a more significant and robust measurement than the soft X-ray lag found in Obs-2.

As an additional check we apply the light-curve folding method to the QPO in Obs-2 ($r_s = 0$ arcsec) and Obs-9. We take the QPO period measured from the entire 0.3–10 keV band as the folding period, which is 3800 s for Obs-2 and 3550 s for Obs-9 (see Section 5.1). The folded light curves are produced for the 0.3–1, 1–4, and 2–10 keV bands, as shown in Fig. 8. Indeed, we also find that the QPO phase in 0.3–1 keV lags behind the 1–4 keV band by 0.024 in Obs-2, while it leads the 1–4 keV band by 0.120 in Obs-9. Interestingly, we find that the QPO phase in 2–10 keV in Obs-2 also leads that for 1–4 keV by 0.044, although the S/N of the 2–10 keV band light curve is much lower. These results are consistent with the QPO lag analysis in the frequency domain.

The opposite time lag between Obs-2 and Obs-9 is difficult to understand. One possible explanation is the influence of the stochastic variability. Figs 7(c) and (d) show that in Obs-2 the coherence in the QPO frequency bin is smaller than the coherence at lower frequencies where the red noise dominates. This leads to the idea that the low-frequency stochastic variability suppresses the coherence in the QPO frequency bin, overwhelms the intrinsic lag of the QPO, and causes the apparent soft lag with a relatively low coherence. In comparison, the low-frequency stochastic variability in Obs-9 is weaker, and so its QPO shows a significant hard lag with a coherence that is much higher than all other frequencies. This red noise contamination can happen if there is a significant aliasing effect of the low-frequency power (Uttley et al. 2014). Additionally, the stochastic variability may also have a physical impact on the QPO properties (Czerny et al. 2010; Hu et al. 2014). Another possibility is the contamination of pile-up. Although it has been shown by Zoghbi & Fabian (2011) and our analysis that the shape of the lag versus frequency spectrum does not change significantly as the S/N decreases, the coherence does decrease significantly as more photons from the centre of the PSF are excluded, and a low coherence often means that the corresponding lag is not reliable. However, it is also possible that the phase lags observed in Obs-2 and Obs-9 are both real, in which case the reversed time lag would be an interesting new phenomenon. In any case, it is crucial to

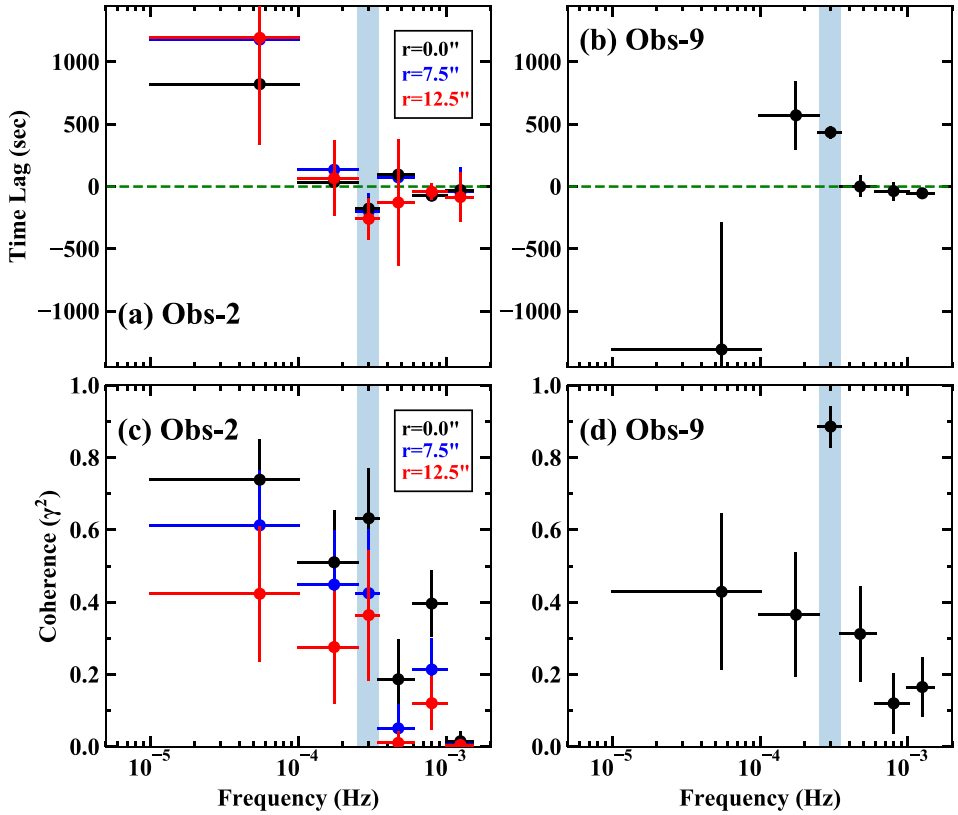


**Figure 7.** Time lag and coherence versus frequency between the light curves in 0.3–1 and 1–4 keV for Obs-2 and Obs-9, separately. In each panel the shadowed region indicates the QPO frequency bin of $(2.5-3.5) \times 10^{-4}$Hz. In (a) and (b), a positive lag means the soft X-ray variability leads the hard X-ray. In (a) and (c), the black, blue, and red data points indicate the results for annular source extraction regions with inner radii being 0, 7.5, and 12.5 arcsec, respectively.

**Table 4.** The coherence and time lag between 0.3–1 and 1–4 keV in the QPO frequency bin of $(2.5-3.5) \times 10^{-4}$ Hz for Obs-2 and Obs-9. $r_s$ indicates different inner radii of the annular source extraction region for checking the pile-up effect. A positive lag indicates that the soft X-ray variability leads the hard X-ray. $N_{data}$ indicates the number of data points in the periodogram being included in the QPO frequency bin.

| Obs | $r_s$ (arcsec) | $N_{data}$ | Time lag (s) | Coherence |
|---|---|---|---|---|
| Obs-2 | 0 | 9 | $-180 \pm 90$ | $0.63 \pm 0.14$ |
| Obs-2 | 7.5 | 9 | $-200 \pm 140$ | $0.42 \pm 0.18$ |
| Obs-2 | 12.5 | 9 | $-260 \pm 160$ | $0.36 \pm 0.18$ |
| Obs-9 | 0 | 7 | $430 \pm 50$ | $0.89 \pm 0.06$ |

carry out further observations in order to understand the true lag behaviours of this QPO.

### 5.3 Anticorrelation between the QPO detectability and the soft X-ray intensity

The trigger of the QPO in RE J1034+396 is still not clear (Middleton et al. 2011). Previous studies have shown that the detection of this QPO is associated with the spectral hardness ratio, as the only two observations showing no QPO signal both have higher soft X-ray fluxes (Alston et al. 2014). To investigate this issue further, we perform simultaneous spectral fitting to all the time-averaged spectra from previous *XMM–Newton* observations, with a typical spectral model of super-Eddington NLS1s which includes absorbed power law and a soft X-ray Comptonization model (e.g. Jin et al. 2017a). The Galactic absorption is fixed at $N_H = 1.36 \times 10^{20}$ cm$^{-2}$ (Willingale et al. 2013), and the intrinsic absorption in RE J1034+396 is left as a free parameter. This model fits the time-averaged spectra very well, with the total $\chi^2$ being 3942 for 3252 dof for all the nine time-averaged EPIC-pn spectra. The slope of the soft excess is characterized by the photon index of a single power law fitted to the 0.3–2 keV spectrum.

The best-fitting $N_H$, fluxes and photon indices are all listed in Table 1. The spectra and their ratios relative to the best-fitting power law above 2 keV are shown in Fig. 9. Note that Obs-1 is an exception because its clean exposure time is only 1.8 ks, and so we do not consider it as a useful data set for the QPO study. In the rest of the observations, Obs-3 and Obs-6 have no QPO signal, and their soft excesses are much stronger and steeper than in other observations where a QPO can be detected. There is no significant difference in the hard X-ray flux or spectral slope between observations with and without a QPO, thus it is not very likely for the hard X-rays to contain the QPO trigger.

This anticorrelation between the QPO detectability and soft X-ray flux also appears consistent with the fact that the fractional rms variability of the QPO in 0.3–1 keV is less than that seen in harder X-rays. However, the soft X-ray fluxes of the two non-QPO observations are only a factor of 2–3 higher than the other QPO observations, so the non-detection of the QPO is not simply due to the dilution from an enhanced non-QPO soft X-ray component. We suggest that there should be some fundamental change in the accretion flow during Obs-3 and Obs-6, which enhances the soft

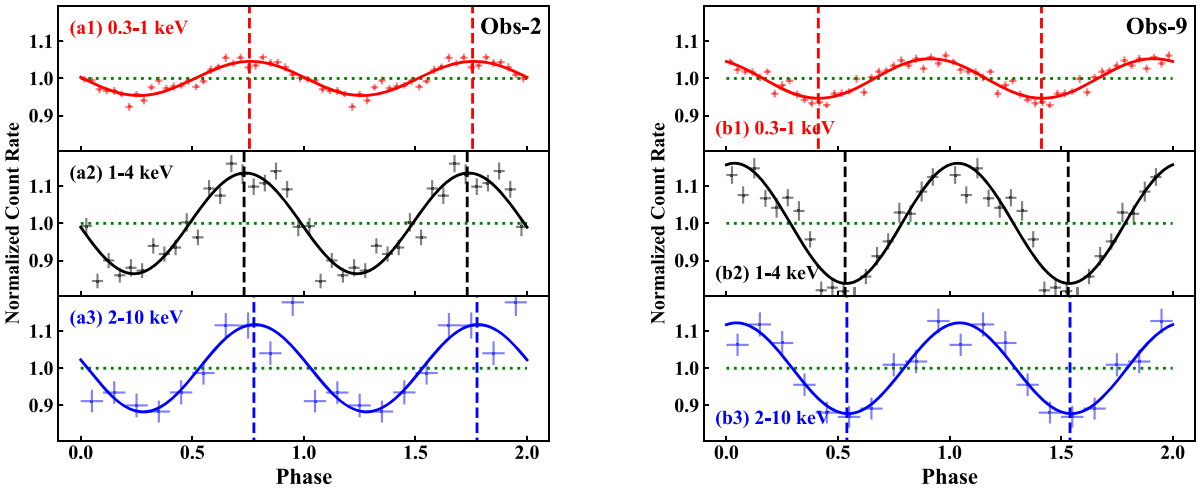


**Figure 8.** Folded QPO light curves of RE J1034+396. (a1)–(a3): folded QPO light curves in Obs-2 with a folding period of 3800 s. Two periods are shown to reveal the periodicity. The best-fitting sinusoidal function with a phase shift are shown by the solid line in each panel. The vertical dash lines indicate the QPO peaks, where phase differences can be found between different energy bands. (b1)–(b3): folded light curves in Obs-9 with a folding period of 3550 s.

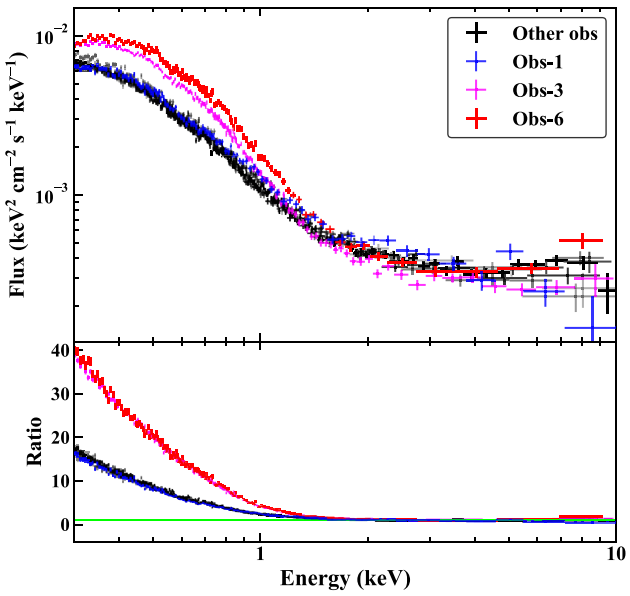


**Figure 9.** The spectra of RE J1034+396 in all the nine *XMM–Newton* observations. The blue, magenta, and red spectra are from Obs-1, Obs-3, and Obs-6, respectively. Spectra from the other observations are presented in different grey-scales as they have similar shapes. The ratio is relative to the best-fitting hard X-ray power-law component. It is clear that Obs-3 and Obs-6, which do not exhibit any QPO signal, have stronger soft X-ray excesses than the other observations with the QPO signal.

X-ray emission and eliminates the QPO signal. This issue will be investigated in more detail in our Paper II.

## 6 DISCUSSION

The strong QPO signal in RE J1034+396 is a rare phenomenon in AGNs, and so its presence raises many interests and questions. Many models have been proposed to explain the QPO mechanism. For example, it was suggested that there is probably an X-ray emitting blob in the accretion flow of RE J1034+396 which is periodically obscured by a warm absorber, so that the QPO signal is produced along with an absorption line whose variation is weakly correlated with the QPO's phase (Maitra & Miller 2010, but also see Middleton, Uttley & Done 2011). In order to explain the correlation between the instantaneous flux and QPO period, other models have been proposed, such as invoking a magnetic flare in a Keplerian orbit which has an intrinsic oscillation (Czerny et al. 2010), an oscillating shock in the accretion flow (Czerny et al. 2010; Das & Czerny 2011; Hu et al. 2014), a spiral wave in a constant rotation state (Czerny et al. 2010), a temporary hotspot carried by the accretion flow with the Keplerian motion (Hu et al. 2014), the g-mode Discoseismology caused by the gravitational-centrifugal force (Hu et al. 2014). However, due to the lack of more detailed characterization of the QPO properties and its long-term variability, all these models remain poorly constrained.

The new results concerning the QPO properties presented in this work have provided tests for some of these theoretical models. First, we now know that this particular QPO is a long-term, recurrent feature of this source, which appears in RE J1034+396 from time to time during the past 11 yr. This result suggests that the QPO is produced by a quite stable mechanism, and so disfavours models involving shorter time-scales. For example, an X-ray emitting blob carried by the accretion flow at $10R_g$ away from a $\sim 10^6$ $M_\odot$ black hole would be accreted into the black hole within just a few months, but we observe a period shortening of only $250 \pm 100$ s over the past 11 yr. So this QPO model can be ruled out with some confidence.

Secondly, now that we have more observational information to examine which energy band produces the QPO. One of the main results is that in Obs-9 the QPO in 0.3–1 keV is leading 1–4 keV by $430 \pm 50$ s with a high coherence. This is more consistent with the possibility that the QPO is driven by a soft X-ray component, although the time lag alone is not sufficient to pin down the causality. This possibility is further supported by the anticorrelation found between the detectability of the QPO and the intensity of the soft X-ray excess, and also by the fact that the absolute rms amplitude of the QPO is larger in 0.3–1 keV than in harder X-ray bands. For comparison, we do not observe any systematic difference of the hard X-ray power law between the time-averaged spectra with and without the QPO (see Table 1). For example, the hard X-ray photon

indices and fluxes of the two non-QPO observations (i.e. Obs-3 and Obs-6) are not significantly different from the QPO observations. Therefore, it seems not likely that the origin of the QPO lies in the hard X-ray band. Moreover, the QPO frequency does not change significantly with the energy bands, so either the QPO-related soft and hard X-ray regions have similar sizes, or the mechanism is such that the QPO time-scale does not depend on the size of its emitting region. One possibility is that the QPO arises from the soft X-ray band, and is transmitted to the hard X-ray band via Comptonization of the QPO modulated soft emission.

Thirdly, the QPO in RE J1034+396 has often been compared to the high-frequency QPOs in the microquasar GRS 1915+105. The similarity between RE J1034+396 and GRS 1915+105 in terms of their X-ray spectra, PSD, and the super-Eddington accretion states suggest that the 67 Hz QPO in GRS 1915+105 may be an analogue of the QPO in RE J1034+396. This was first proposed by Middleton et al. (2009) (also see Middleton, Uttley & Done 2011; Done 2014), but the (apparent) soft X-ray lag in the Obs-2 data is opposite to the soft X-ray lead seen in the 67 Hz high frequency QPO in GRS 1915+105 (Méndez et al. 2013), thereby breaking the scaling relation. However, as we point out in this work, the associated coherence of the QPO time lag is low in 2007, so the soft lag is not very significant in these data, especially after the pile-up correction. Instead, our new data from Obs-9 show that the highly coherent QPO in RE J1034+396 has a soft X-ray lead, strongly supporting the analogy to the 67 Hz QPO in GRS 1915+105. Other features of the QPO are also consistent, e.g. small but significant changes in the 67 Hz QPO frequency are also seen in GRS 1915+105 (Belloni et al. 2019), similar to the fractional change in QPO frequency seen in RE J1034+396 when comparing Obs-2 and Obs-9. The lack of a harmonic signal in RE J1034+396 is not a concern, because the 'harmonic' features in GRS 1915+105 do not appear simultaneously with the 67 Hz QPO very often, and they are all significantly weaker than the 67 Hz QPO (Méndez et al. 2013).

So what then is the origin of the 67 Hz QPO in GRS 1915+105? These high frequency QPOs are rare in BHB, but are much more common in neutron star X-ray binaries (XRBs). In these objects we generally see two QPOs in the kHz region, an upper and a lower frequency separated by a few hundred Hz (see e.g. the review by van der Klis 2006). The lower frequency QPO shows a soft X-ray lag, while the upper frequency one generally shows a soft X-ray lead (de Avellar et al. 2013; Peille et al. 2015; Troyer et al. 2018). The (very rare) BHB high frequency QPOs are probably the counterpart of the upper frequency QPO in neutron star XRBs (Méndez et al. 2013). These are likely produced by oscillations within the Comptonizing boundary layer between the disc and neutron star (Gilfanov et al. 2003; see also Karpouzas et al. 2020 for a detailed model of the lower frequency QPO). Whatever their origin is, we conclude that the QPO of RE J1034+396 is indeed similar to the 67 Hz QPO in GRS 1915+105, where the soft X-rays lead the hard X-rays (Méndez et al. 2013).

## 7 CONCLUSIONS

In this paper, we report the detection of a strong X-ray QPO in the new *XMM–Newton* observation of RE J1034+396 in 2018, which is separated by 7 yr from the previous *XMM–Newton* observation and 11 yr from the original discovery of this QPO signal. New and detailed analysis have been conducted that verify and extend the QPO properties previously known, which are summarized below:

(i) we confirm that the X-ray QPO in RE J1034+396 is a robust phenomenon which has occurred, at least intermittently, for more than 11 yr. Its presence is most significant in the latest observation taken in 2018, which yields a $9\sigma$ significance of detection in the 1–4 keV band. The quality value is ∼20, and the folded light curve exhibits a well-defined sinusoidal shape, and so the QPO is highly coherent.

(ii) in the new Obs-9 data the QPO period is found to be $3530 \pm 80$ s in the 1–4 keV band, and shows no significant change with energy bands. However, the fractional rms of the QPO increases from 4 per cent in 0.3–1 keV to 12.4 per cent in the 1–4 keV band, although the absolute rms amplitude of the QPO in 0.3–1 keV is actually a factor of 2.4 higher than in the 1–4 keV band.

(iii) we find that the QPO period is shorter in the new observation than was observed before. It was $3800 \pm 70$ s in the 1–4 keV light curve in Obs-2, but decreases by $250 \pm 100$ s in Obs-9 (i.e. ∼7 per cent of the QPO period). The significance of this long-term variation of the QPO period is also confirmed by our simulations performed following the Bayesian approach.

(iv) our analysis shows that the QPO the 0.3–1 keV band leads the 1–4 keV band by $430 \pm 50$ s, and the time lag is accompanied by a high coherence. This result is further confirmed by the direct folding of the light curves in these energy bands. This soft X-ray lead is opposite to the soft X-ray lag reported previously for Obs-2. However, our reanalysis of these data indicates that the QPO lag found in Obs-2 is associated with a lower coherence, and so it is less robust than that observed in Obs-9. Therefore, either the previously reported soft X-ray lag is not intrinsic to the QPO, or the lag has changed direction from Obs-2 to Obs-9, which if confirmed would be an interesting new phenomenon to explain. Clearly future observations are required to address this issue.

(v) by analysing the data from all previous *XMM–Newton* observations, we show that the two observations without a QPO show stronger soft X-ray excesses than the other observations which display evidence of a QPO. Therefore, we conclude that there is a long-term anticorrelation between the intensity of the soft X-ray excess and the detectability of a QPO signal.

These newly discovered and refined properties of the QPO in RE J1034+396 show that it is more similar to the 67 Hz QPO in GRS 1915+105. We also suggest that the QPO of RE J1034+396 is probably driven by a soft X-ray component. In order to further understand the mechanisms of the QPO and the soft excess, we will present a more comprehensive spectral-timing analysis for the QPO together with broader frequency ranges in our forthcoming Paper II. Finally, we emphasize the importance of carrying out long-term monitoring of the QPO and the spectral state of RE J1034+396. This source provides one of the best laboratories in which to study the physics of the QPO phenomenon in AGNs, and so we recommend it to be one of the highest priority AGN targets for future X-ray missions such as the Einstein Probe mission (*EP*), the enhanced X-ray Timing and Polarimetry mission (*eXTP*), and the Advanced Telescope for High-ENergy Astrophysics (*Athena*).

## ACKNOWLEDGEMENTS

We thank the anonymous referee for providing useful comments to improve the paper. CJ acknowledges the National Natural Science Foundation of China through grant 11873054, and the support by the Strategic Pioneer Program on Space Science, Chinese Academy of Sciences through grant XDA15052100. CD and MJW acknowledge the Science and Technology Facilities Council (STFC)

through grant ST/P000541/1 for support. This work is based on observations conducted by *XMM–Newton*, an ESA science mission with instruments and contributions directly funded by ESA Member States and the USA (NASA). This research has made use of the NASA/IPAC Extragalactic Database (NED) which is operated by the Jet Propulsion Laboratory, California Institute of Technology, under contract with the National Aeronautics and Space Administration.

## REFERENCES

Alston W. N., Done C., Vaughan S., 2014, MNRAS, 439, 1548
Alston W. N. et al., 2015, MNRAS, 449, 467
Arnaud K. A., 1996, in Jacoby G. H., Barnes J., eds, ASP Conf. Ser. Vol. 101, Astronomical Data Analysis Software and Systems V. Astron. Soc. Pac., San Francisco, p. 17
Belloni T. M., Altamirano D., 2013, MNRAS, 432, 19
Belloni T., Hasinger G., 1990, A&A, 230, 103
Belloni T., Méndez M., Sánchez-Fernández C., 2001, A&A, 372, 551
Belloni T. M., Bhattacharya D., Caccese P., Bhalerao V., Vadawale S., Yadav J. S., 2019, MNRAS, 489, 1037
Bian W. H., Huang K., 2010, MNRAS, 401, 507
Carpano S., Jin C., 2018, MNRAS, 477, 3178
Casebeer D. A., Leighly K. M., Baron E., 2006, ApJ, 637, 157
Chaudhury K. et al., 2018, MNRAS, 478, 4830
Crummy J., Fabian A. C., Gallo L., Ross R. R., 2006, ApJ, 365, 1067
Czerny B., Lachowicz P., Dovčiak M., Karas V., Pecháček T., Das T. K., 2010, A&A, 524, A26
Czerny B. et al., 2016, A&A, 594, A102
Das T. K., Czerny B., 2011, MNRAS, 414, 627
de Avellar M. G. B., Méndez M., Sanna A., Horvath J. E., 2013, MNRAS, 433, 3453
Done C., 2014, in Ishida M., Petre R., Mitsuda K., eds, Expanding the Frontiers of the X-ray Universe, proc. conf. Suzaku-MAXI 2014, p. 300
Done C., Jin C., 2016, MNRAS, 460, 1716
Done C., Davis S. W., Jin C., Blaes O., Ward M., 2012, MNRAS, 420, 1848
Gierliński M., Middleton M., Ward M., Done C., 2008, Nature, 455, 369
Gilfanov M., Revnivtsev M., Molkov S., 2003, A&A, 410, 217
Gonçalves A. C., Véron P., Véron-Cetty M. P., 1999, A&A, 341, 662
Gupta A. C., Tripathi A., Wiita P. J., Gu M., Bambi C., Ho L. C., 2018, A&A, 616, L6
Hogg D. W., Bovy J., Lang D., 2010, preprint (arXiv:1008.4686)
Hu C.-P., Chou Y., Wu M. C., Yang T. C., Su Y. H., 2011, ApJ, 740, 67
Hu C. P., Chou Y., Yang T. C., Su Y. H., 2014, ApJ, 788, 31
Huang N. E. et al., 1998, Proc. R. Soc. A, 454, 903
Ingram A., Done C., Fragile P. C., 2009, MNRAS, 397, L101
Jansen F. et al., 2001, A&A, 365, L1
Jin C., Ward M., Done C., Gelbord J., 2012a, MNRAS, 420, 1825
Jin C., Ward M., Done C., 2012b, MNRAS, 422, 3268
Jin C., Ward M., Done C., 2012c, MNRAS, 425, 907
Jin C., Done C., Middleton M., Ward M., 2013, MNRAS, 436, 3173
Jin C., Done C., Ward M., 2016, MNRAS, 455, 691
Jin C., Done C., Ward M., 2017a, MNRAS, 468, 3663
Jin C., Done C., Ward M., 2017b, MNRAS, 471, 706
Karpouzas K., Méndez M., Ribeiro E. M., Altamirano D., Blaes O., García F., 2020, MNRAS, 492, 1399
Lin D., Irwin J. A., Godet O., Webb N. A., Barret D., 2013, ApJ, 776, L10
Maitra D., Miller J. M., 2010, ApJ, 718, 551
Mason K. O., Puchnarewicz E. M., Jones L. R., 1996, MNRAS, 283, L26
McHardy I. M., Koerding E., Knigge C., Uttley P., Fender R. P., 2006, Nature, 444, 730
McHardy I. M., Arévalo P., Uttley P., Papadakis I. E., Summons D. P., Brinkmann W., Page M. J., 2007, MNRAS, 382, 985
Méndez M., Altamirano D., Belloni T., Sanna A., 2013, MNRAS, 435, 2132
Middleton M., Done C., 2010, MNRAS, 403, 9
Middleton M., Done C., Ward M., Gierliński M., Schurch N., 2009, MNRAS, 394, 250
Middleton M., Uttley P., Done C., 2011, MNRAS, 417, 250
Miniutti G. et al., 2019, Nature, 573, 381
Pan H. W., Yuan W., Yao S., Zhou X. L., Liu B., Zhou H., Zhang S. N., 2016, ApJ, 819, L19
Pasham D. R. et al., 2019, Science, 363, 531
Peille P., Barret D., Uttley P., 2015, ApJ, 811, 109
Puchnarewicz E. M., Mason K. O., Siemiginowska A., Pounds K. A., 1995, MNRAS, 276, 20
Reid M. J., McClintock J. E., Steiner J. F., Steeghs D., Remillard R. A., Dhawan V., Narayan R., 2014, ApJ, 796, 2
Reis R. C., Miller J. M., Reynolds M. T., Gültekin K., Maitra D., King A. L., Strohmayer T. E., 2012, Science, 337, 949
Remillard R. A., McClintock J. E., 2006, ARA&A, 44, 49
Shu X. W., Wang S. S., Dou L. M., Jiang N., Wang J. X., Wang T. G., 2018, ApJ, 857, L16
Stella L., Vietri M., 1998, ApJ, 492, L59
Strohmayer T. E., 2001, ApJ, 554, L169
Strüder L. et al., 2001, A&A, 365, L18
Troyer J. S., Cackett E. M., Peille P., Barret D., 2018, ApJ, 860, 167
Uttley P., Cackett E. M., Fabian A. C., Kara E., Wilkins D. R., 2014, A&AR, 22, 72
van der Klis M., 2006, Adv. Space Res., 38, 2675
Vaughan S., 2010, MNRAS, 402, 307
Vaughan S., Uttley P., 2005, MNRAS, 362, 235
Vaughan S., Uttley P., 2006, Adv. Space Res., 38, 1405
Veledina A., Poutanen J., Ingram A., 2013, ApJ, 778, 165
Wang J. M., Netzer H., 2003, A&A, 398, 927
Willingale R., Starling R. L. C., Beardmore A. P., Tanvir N. R., O'Brien P. T., 2013, MNRAS, 431, 394
Wu Z., Huang N. E., 2009, Advances in Adaptive Data Analysis, 1, 1
Zhang P., Zhang P. F., Yan J. Z., Fan Y. Z., Liu Q. Z., 2017, ApJ, 849, 9
Zhang P. F., Zhang P., Liao N. H., Yan J. Z., Fan Y. Z., Liu Q. Z., 2018, ApJ, 853, 193
Zoghbi A., Fabian A. C., 2011, MNRAS, 418, 2642

This paper has been typeset from a TEX/LATEX file prepared by the author.